Indonesian Journal of Green Chemistry
E-ISSN: 3064-4720
DOI: https://doi.org/10.69930/ijgc.v2i2.627
Research Article

Vol. 2 (2), 2025
Page: 109-122

Modeling of the Layered Hydraulic Fracturing Process for Enhanced Reservoir Performance

Shirullah Rahmani *, **Nasratullah Mahboob**, **Ruhullah Hanif**

Deparment of Chemistry, Education faculty, Samangan University, Aibak, Samangan, Afghanistan
*Email (corresponding author): shirullahrahmanyar500@gmail.com

Abstract. *Over the past decade, the Tanatar oil and gas field has experienced a marked decline in output, underscoring the critical demand for effective well stimulation strategies to restore reservoir productivity. The core problem addressed in this study is the falling performance of mature wells and the absence of detailed modeling research that evaluates hydraulic fracturing within the field's unique geological context. This research examines the application of hydraulic fracturing through an advanced numerical modeling framework designed to simulate key physical processes. This includes the dynamics between particles, the initiation and propagation of fractures, and the interactions between fluids and the solid rock matrix. By integrating a discrete-element method with fluid flow simulation, the model captures the microscale mechanisms that govern fracturing. After being calibrated using authentic reservoir data from the field, the computational model was used to analyze stress fields, fracture network growth, pressure changes over time, and the corresponding enhancements in permeability. The modeling framework allows for accurate forecasting of both fracture geometry and overall reservoir performance under various operational conditions. Findings indicate that hydraulic fracturing significantly improves permeability within the Tanatar field's underperforming zones, thereby boosting wellbore deliverability. The simulations reveal clear relationships between fluid injection pressure, the direction and pattern of fracture growth, and the total volume of reservoir rock that is effectively stimulated. Furthermore, the analysis demonstrates that hydraulic fracturing presents a viable and controlled method for extending the commercial viability of depleted reservoirs. In summary, this work provides the first comprehensive numerical investigation of hydraulic fracturing's potential for the Tanatar field, establishing it as a highly promising technique for enhancing production. The insights derived offer practical guidance for field operations and strengthen the case for adopting hydraulic fracturing as a reliable stimulation method in analogous low-permeability reservoirs.*

Keywords: *Hydraulic fracturing, numerical modeling, permeability, reservoir simulation, well productivity*

1. Introduction

Volatile Organic Compounds (VOCs) and subsurface geomechanical processes are recognized as two critical areas of research within environmental science and petroleum engineering. VOCs represent a significant threat to atmospheric quality and public health, particularly in densely populated and industrialized zones (Caselli et al., 2010; Khoder, 2007). Investigations across various metropolitan areas—including Beijing, Jeddah, Cairo, and Yokohama—have consistently identified elevated concentrations of hazardous BTEX compounds (Benzene, Toluene, Ethylbenzene, Xylene), primarily originating from vehicular traffic, industrial emissions, and specific meteorological conditions (Gee & Sollars, 1998; Grosjean, 1998; Li et al., 2010; Alghamdi et al., 2014). Given their documented short- and long-term health impacts, regulatory bodies such as the U.S. Environmental Protection Agency have developed comprehensive frameworks for assessing associated risks (U.S. EPA, 2009; DEFRA, 2012).

Received: 30 September 2025 / Accepted: 30 October 2025 / Available online: 31 October 2025

Accurate detection and quantification of these airborne contaminants are therefore essential for effective air quality management. Advances in sampling and analytical technologies—such as solid-phase microextraction (SPME), diffusive samplers, and specialized trapping devices—have substantially improved measurement sensitivity, reproducibility, and field applicability (Pawliszyn, 1997; Gelencsér et al., 1994). More recent innovations, including time-weighted SPME and advanced silica-based traps, now enable reliable long-term monitoring under varying environmental conditions, allowing for high-resolution mapping of emission sources across complex urban landscapes (Khaled & Pawliszyn, 2000; Caselli et al., 2010).

In parallel, geomechanical analysis of fractured rock formations has become equally vital for applications in geothermal energy, hydraulic fracturing, and reservoir engineering. The interplay between in-situ stresses, natural fault networks, and fluid injection governs key subsurface behaviors, including permeability enhancement and induced seismicity (Davatzes, 2012; Häring et al., 2008). Research indicates that pre-existing fractures can either promote or impede fluid flow depending on their orientation, mechanical properties, and the prevailing stress regime (Gale & Holder, 2005; Gu & Weng, 2003). Understanding fault stability and slip mechanisms is therefore crucial for predicting subsurface responses to fluid injection, as evidenced by pore-pressure-triggered seismic events documented at sites such as Basel's HotFract project (Dieterich, 2008; Cuenot & Frogneux, 2011).

Discrete Fracture Network (DFN) modeling has emerged as a powerful tool for simulating hydraulic fracture propagation within naturally fractured reservoirs (Hartman et al., 2014). The interaction between newly induced and pre-existing fractures directly influences stimulation effectiveness, fracture geometry, and resultant permeability pathways (Laowagul & Yoshizumi, 2009). Optimizing this interaction is key to maximizing hydrocarbon recovery while mitigating environmental risks, such as subsurface gas migration and induced seismicity (Genter, 1973; Fetterman & Davatzes, 1994).

Despite considerable progress in subsurface deformation modeling, research integrating these advances with atmospheric VOC monitoring remains limited. Deteriorating urban air quality, especially in high-traffic corridors with inadequate emission controls, underscores the need for enhanced, long-term monitoring methodologies (Gee & Sollars, 1998; Alghamdi et al., 2014). Simultaneously, field-scale predictive modeling in geomechanics continues to face challenges related to accurately simulating fracture propagation, stress evolution, and dynamic permeability changes (Gulrajani & Nolte, 1971; Downie, 2004).

2. Methods

This study employs a numerical modeling approach to analyze hydraulic fracturing within a multilayered reservoir system under varying geomechanical and operational conditions. The investigation utilizes a Discrete Element Method (DEM) framework capable of simulating fracture initiation, propagation, and interaction with reservoir heterogeneities. The model integrates mechanical deformation with fluid flow processes within a fully coupled hydro-mechanical system.

A six-layered reservoir geometry was constructed based on calibrated data from published literature, with distinct mechanical properties—including elastic modulus, tensile strength, cohesion, and fracture toughness—assigned to each layer. Interfacial properties between layers were explicitly defined to capture stress contrasts and potential delamination. Fluid injection was simulated via a pore-pressure diffusion algorithm, which transfers hydraulic forces to particle contacts, thereby initiating and driving fracture growth. A time-stepping numerical scheme was applied to track particle displacement and stress redistribution during injection, with local and viscous damping used to ensure computational stability. The model was calibrated and validated against established analytical solutions and experimental results to verify the accuracy of simulated fracture patterns.

3. Results and Discussion

Based on the Discrete Element Method (DEM) simulation, the model's left boundary was defined as a fixed wellbore wall. Fluid was introduced at a central injection point within this boundary. This setup eliminated the need to explicitly model a perforation, as the initial fracture nucleation occurred naturally within the inherent microscopic gaps between bonded particles.

A constant-rate fluid injection into the porous assembly led to a gradual buildup of pore pressure. Fracture initiation commenced only when the fluid-induced forces overcame the in-situ confining stresses. Within the bonded particle matrix, micro-cracks developed at particle contacts where the bonding strength was exceeded. Tensile cracks formed when the normal bond strength was surpassed, while shear cracks resulted from exceeding the shear bond strength (Gale & Holder, 2005). These discrete micro-cracks subsequently coalesced to form macroscopic fractures.

The propagation of fractures was monitored through pressure-history analysis. Under a constant injection rate, fluctuations in the recorded injection pressure corresponded directly to key physical processes: fluid infiltration into new pores, dilation of the rock matrix, and the extension of fracture tips. Step-wise increases in the injection velocity produced corresponding jumps in the pressure profile.

Prior to injection, the particle assembly was in a state of compressive stress. The introduction of fluid generated localized tensile forces around the injection point, which reduced the contact forces between particles and initiated cracking. Upon reaching a critical pressure threshold, the contact forces near the injection node effectively diminished to zero, marking the definitive initiation of a fracture cavity (Lee et al., 2002).

The evolution of contact forces during the simulation is illustrated in Figure 5. This visualization confirms observations from Figures 1-4, which show a high density of tensile cracks forming near the injection inlet. As demonstrated in Figure 5, the stress state of particles adjacent to the injection point transitions from compressive to tensile immediately prior to fracture initiation.

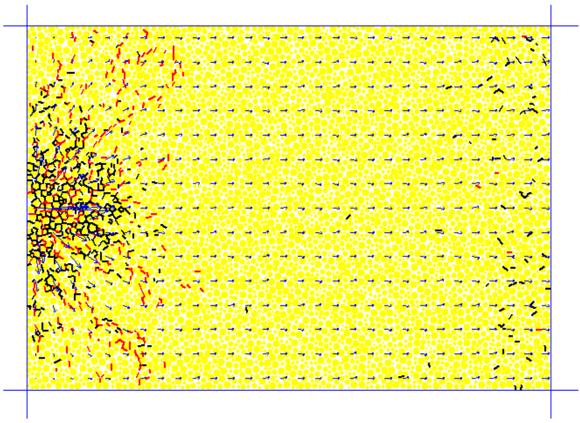

Figure 1. Normal (red) and Shear (black) cracks (v_{lnk}=100 m/s)

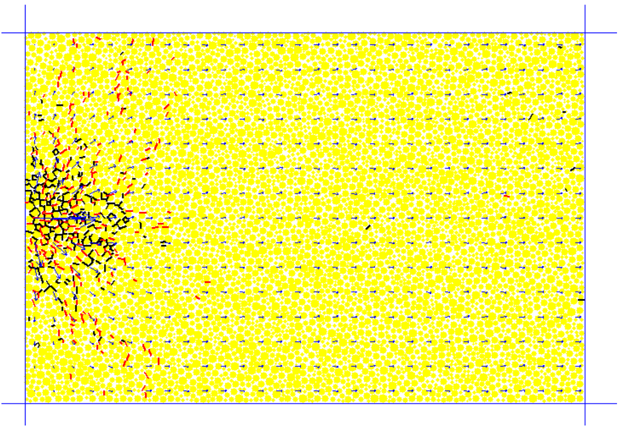

Figure 2. Normal (red) and Shear (black) cracks (v_{lnk} =75 m/s)

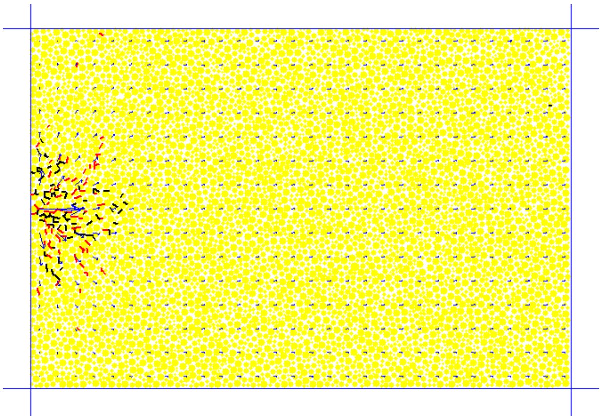

Figure 3. Normal (red) and Shear (black) cracks (v_{lnk}=50 m/s)

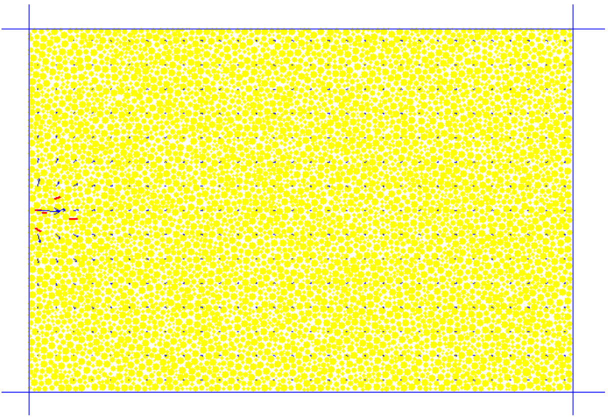

Figure 4. Normal (red) and Shear (black) cracks (v_{lnk}=25 m/s)

The pressure-time curve derived from the simulation reveals three distinct stages of hydraulic fracture development: cavity initiation, even cavity propagation, and uneven cavity propagation.

The initial phase is marked by a linear increase in pressure at a constant slope, representing the elastic compression of the rock matrix and the buildup of pore pressure prior to failure. A distinct change in the slope of this curve signals the onset of fracture initiation. This point is followed by a peak pressure, after which the slope decreases, indicating the transition to uneven, branching fracture growth.

The mechanical interpretation of this curve can be summarized as follows: the initial linear segment corresponds to elastic deformation, the peak pressure denotes fracture initiation, and the subsequent pressure drop characterizes the unstable propagation phase. During the period of even propagation, the applied pressure is sufficient to hold fractures open and extend their length uniformly, often at a relatively constant pressure. Once propagation becomes uneven, the pressure fluctuates as the fracture navigates heterogeneities and branches into the formation.

This interpretation is supported by monitoring the internal contact forces between particles. Prior to fracture, the assembly exhibits high, stable contact forces, indicating an intact, load-bearing matrix. Immediately following fluid injection, these contact forces drop significantly (as seen in Figure 5b) due to rapid fluid permeation and the reduction of effective stress. However, they quickly rebuild (Figure 5c), reflecting a re-establishment of particle contacts in response to confining boundary conditions and the redistribution of stresses from fluid drag forces (Evans et al., 2012).

An idealized schematic of this pressure evolution is presented in Figure 6. It illustrates the initial linear pressure buildup, the inflection point at cavity initiation where the slope begins to flatten, and the peak where the slope reaches zero before declining.

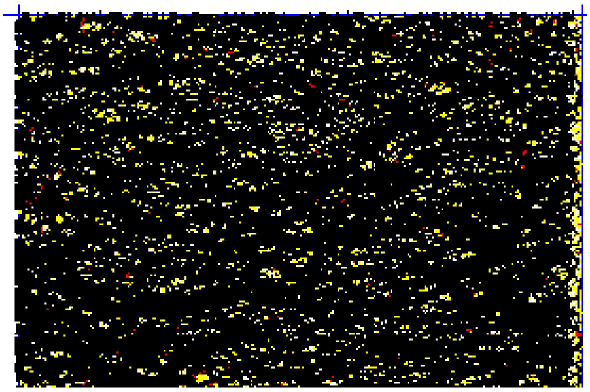

Figure 5a. Contact force distribution before fluid injection

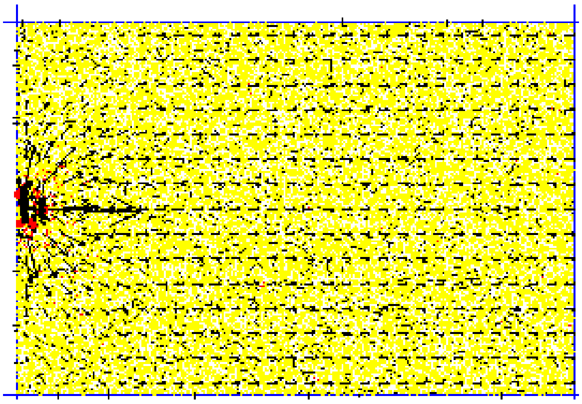

Figure 5b. Force distribution immediatelyafter fluid injection

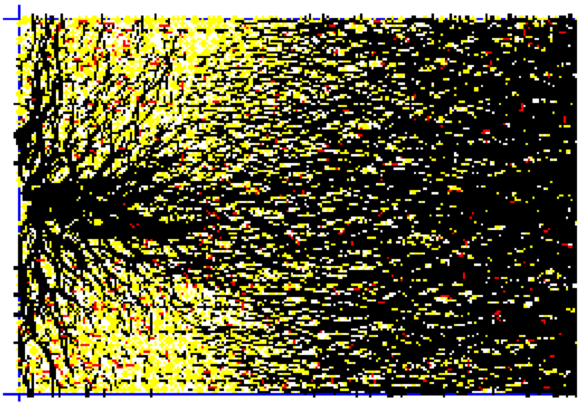

Figure 5c. Increasing contact forces due to boundary conditions and drag forces

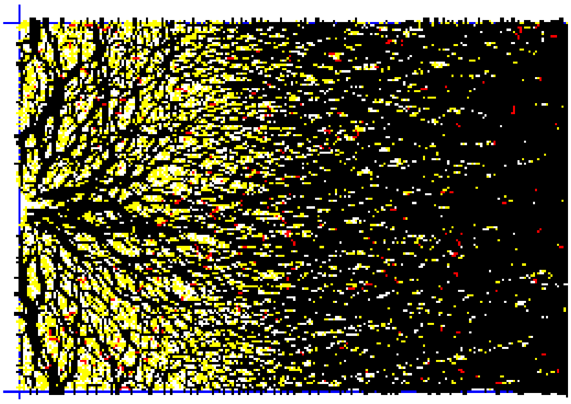

Figure 5d. Contact force distribution towards the end of simulation period (v_{lnk} =100 m/s)

Fracture Initiation and Cavitation Mechanics

In this model, fracture initiation is defined by the initial breakdown of interparticle bonds—either in shear or tension—within the bonded bulk material. Cavitation, however, is a distinct subsequent phase. It occurs during fluidization when fluid drag forces overcome the net effect of buoyancy and gravitational forces on particles. This process loosens the particle assembly, driving the effective stress toward zero as pore pressure approaches the total confining stress. Critically, for bonded materials, fracture must precede displacement and cavitation, unlike in granular systems where hydraulic fracture and cavitation onset are concurrent. For the purpose of this study, cavitation initiation is specifically identified when the maximum ratio of particle displacement (in the x-direction) to particle diameter exceeds 0.1.

Numerical Methodology and Validation

To address numerical challenges inherent in modeling dense particle assemblies, the simulation employed very small mechanical and fluid timesteps to ensure convergence and accuracy. To efficiently elicit a system response within this framework, elevated fluid injection velocities were utilized—a common compensatory technique in such numerical experiments (Fetterman & Davatzes, 1994). The pressure histories generated across various injection velocities, shown in Figure 6 (a-b), demonstrate a reinforcement pattern consistent with established literature.

The modeled pressure-time curve exhibits three characteristic stages, as illustrated in the idealized schematic of Figure 6:

1. **Pre-initiation Inflation:** A linear pressure buildup prior to the slope break.
2. **Even Propagation:** A period of stable growth following initiation.
3. **Uneven Propagation:** A stage marked by a negative slope, indicating branching and complex fracture growth.

These stages are clearly identifiable in the DEM results presented in Figure 5. The model's validity is further supported by a strong resemblance to physical fracture experiments conducted on layered formations (e.g., Bedford limestone and less permeable Kasota limestone). As demonstrated by Gale and Holder (2005), monitoring pressure as a function of injected volume—an indirect measure of fracture length—reveals comparable trends in pressure reinforcement between the experimental and simulation results, confirming the model's predictive capability for fracture propagation dynamics.

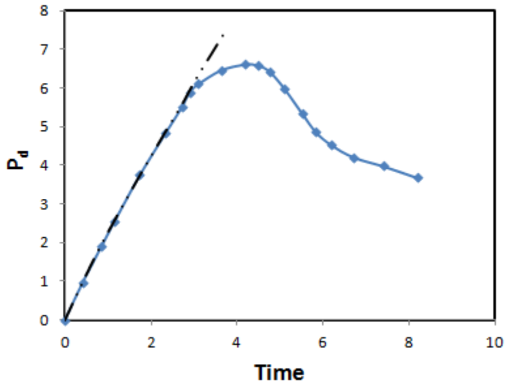

Figure 6a. Idealised record of driving pressure as a function of time

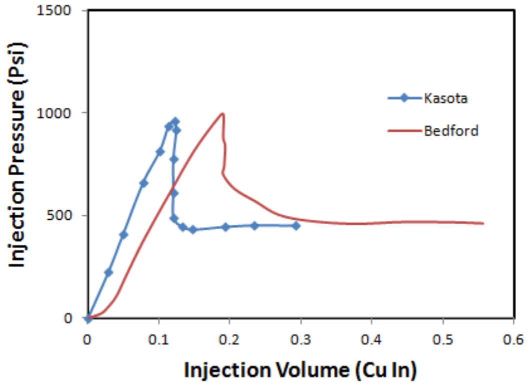

Figure 6b. Experimental records of pressure showing fracture propagation

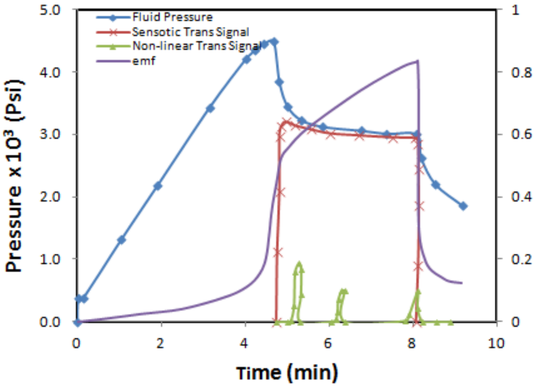

Figure 6c. Record of injection pressure, capacitance bridge emf, pressure transducer signals during typical fracturing experiment

Cavity growth model and cavity initiation criterion

To establish a cavity initiation criterion, two distinct sets of simulations were performed on discrete granular formations. The first set replicated the procedure used for bulk assemblies, employing a constant fluid injection velocity. The second set implemented a stepwise increase in injection velocity until a critical threshold for cavity formation was identified.

At low injection velocities, the fluid-induced drag forces are insufficient to overcome interparticle friction and cohesion. Consequently, the system reaches a state of equilibrium where pressure builds to a stable plateau without causing significant particle displacement or cavity formation. It is theorized that intense infrasonic and ultrasonic vibrations inherent to such pressurized systems may contribute to maintaining this metastable state by inducing micro-scale turbulence and resonant effects within the granular matrix (Gu & Weng, 2003).

As the injection velocity increases incrementally, a critical point is reached where the combined drag forces and driving pressure exceed the resisting forces. This initiates particle mobilization, marking the onset of cavity formation and subsequent unstable growth.

Figure 9 (a-b) presents results from the first test set, depicting the state of cavity development at 60 μs for different injection velocities. The images illustrate that while cavity growth is initially unstable, the system transitions to a period of stabilization governed by fluid pressure. This stabilization phase is clearly identifiable in the pressure-time history as a plateau where the pressure maintains a near-constant value, indicating a temporary balance between injection energy and the mechanical resistance of the formation.

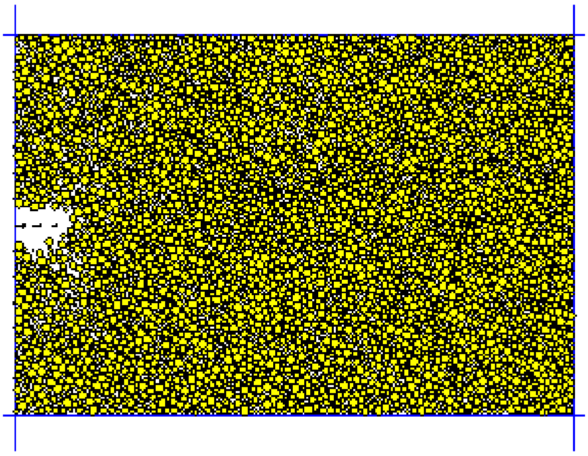

Figure 7a. State of granular material: v_{lnk} =25 m/s

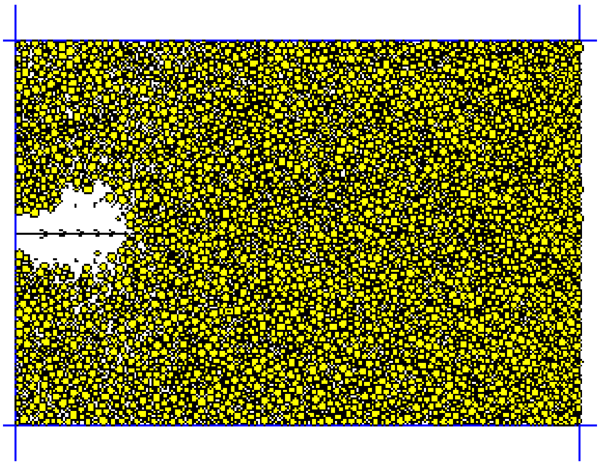

Figure 7b. State of granular material: v_{lnk}=60 m/s

Received: ……. / Accepted: ….. / Available online: ……

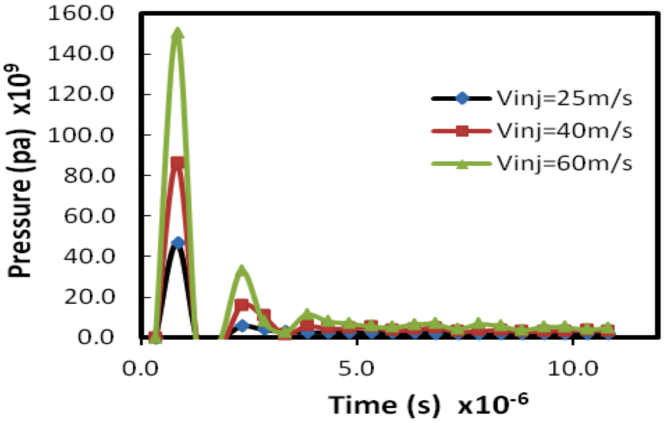

Figure 8. Records of injection pressures at varying constant velocities

Analysis of Injection Pressure and Critical Velocities

The pressure response of the system under different injection conditions is presented in Figures 8-9. Figure 8 illustrates the generated injection pressure profiles over simulation time for various constant fluid velocities.

A subsequent series of tests employed a stepwise increase in injection velocity during a single simulation run. The initial velocity was set at 135 m/s and was incrementally raised to 154 m/s, 229 m/s, 340 m/s, 395 m/s, and finally 445 m/s. Analysis of the results indicates that cavity initiation began at approximately 2.3×10−62.3×10−6 s, with the first critical interstitial velocity (at the injection front) identified as 318 m/s. A second, higher critical velocity—associated with the transition from stable to unstable cavity propagation—was anticipated but not reached, as the simulation was terminated at 4.8×10−44.8×10−4 s. The dynamic interplay between the applied fluid pressure and the evolving interstitial velocity throughout this test is detailed in Figure 9.

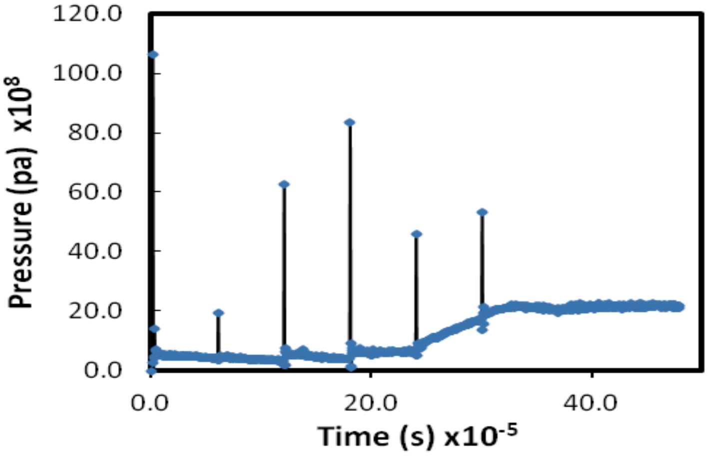

Figure 9. Pressure history as fluid injection velocity is increased due to the timespan

At the second to the last increment of injection velocity, the corresponding interstitial velocity remained constant and close in value to the respective injection velocity (Figure 10), making it evident that the injection front was devoid of particles.

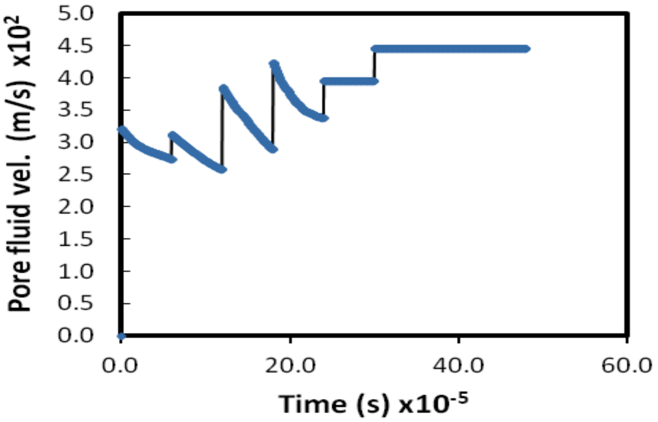

Figure 10. Evolution of interstitial velocity at injection front

Effect of wellbore depth of the reservior

Increased sand production started somewhere near a vertical pressure of 34 MPa and peaked when subjected to a vertical pressure of 103 MPa, as evident from fewer distinct differences in the deformation extent at vertical pressures of 34 MPa and 103 MPa (Figure 11).

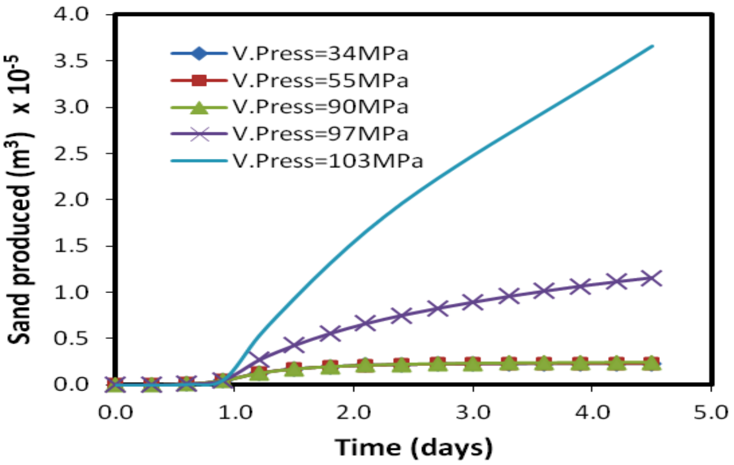

Figure 11. Sand production with increasing vertical pressure

Erosion criteria of the equivalent strain parameter

As previously defined, the onset of erosion was governed by a macro-scale strain parameter. Material removal was stipulated to occur when the equivalent plastic strain within the formation exceeded a predetermined, non-zero threshold. Parametric analysis revealed an inverse relationship between this threshold value and sand production: lower critical strain values resulted in significantly greater volumetric erosion. As illustrated in Figure 15, the most pronounced increase in sand production occurs when the strain criterion is reduced to 1.0. This finding underscores the necessity of establishing a more physically realistic and measurable criterion for erosion initiation, a goal that will require calibration against laboratory experiments in future work.

A second vital component of the erosion study was evaluating the effectiveness of wellbore pressure. This pressure, analogous to the "mud pressure" used in field operations to maintain wellbore stability, was applied at the perforation face. Its magnitude was varied systematically while keeping all other simulation conditions constant.

The results, also depicted in Figure 15, demonstrate a dramatic, non-linear relationship. The volume of eroded sand decreases sharply as mud pressure increases. However, this trend exhibits a clear point of diminishing returns. Beyond approximately 37.2 MPa, further increases in pressure yield negligible additional reductions in sand production. This identifies 37.2 MPa as the effective optimal mud pressure under the simulated conditions, beyond which operational benefits become minimal.

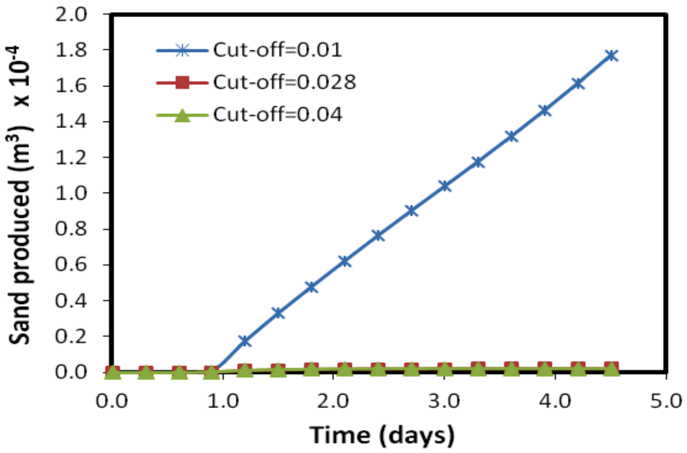

Figure 12a. Effect of erosion criterion on sand production

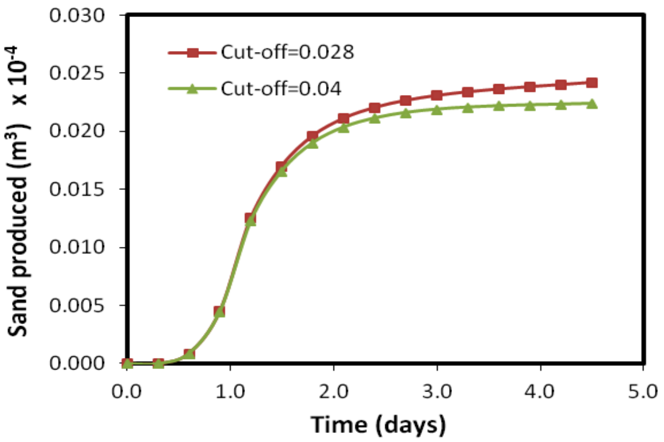

Figure 12b. Effect of erosion criterion on sand production (Comparing cut-off values of 0.028 and 0.04)

Conclusion

This study developed and applied a discrete-element hydraulic fracturing model to a multi-layered reservoir system. The model successfully captured the complex, coupled hydro-mechanical processes governing fracture initiation and propagation, cavity formation, and subsequent sand production.

The simulation results demonstrate that fracture behavior in layered formations is critically influenced by operational parameters—notably injection velocity—and intrinsic material properties, such as interparticle bonding strength. The dynamic redistribution of contact forces during fluid intrusion was shown to control the fracture mode. At lower injection rates, fractures were predominantly tensile (Mode-I). As the velocity increased, the failure mechanism transitioned to a mixed-mode behavior, with a significant shear component.

The model delineated a consistent sequence of events: initial bond breakage, fracture propagation, cavity initiation, and unstable cavity growth. The derived pressure-history curves exhibited the characteristic three-stage pattern (linear buildup, peak, and decline) widely documented in experimental literature, validating the DEM approach for simulating fluid-driven fracturing. A critical interstitial velocity of approximately 318 m/s was identified as the threshold for effective cavity formation, which occurred only after sufficient particle displacement and pressure buildup.

Beyond fracture mechanics, the study highlights key factors affecting long-term well performance. Sand production was shown to be highly sensitive to the in-situ vertical stress and the defined erosion criterion (based on equivalent plastic strain). Furthermore, wellbore stabilization pressure (analogous to mud pressure) is a vital operational control, with simulations indicating an optimal threshold near 37.2 MPa, beyond which additional increases yield diminishing returns in sand suppression.

In summary, this modeling framework effectively replicates the essential microscale mechanisms of hydraulic fracturing in stratified reservoirs. It demonstrates clear sensitivity to both injection strategy and the reservoir stress environment, providing valuable insights for optimizing stimulation designs and mitigating sand production to enhance the long-term productivity of depleted fields. This work establishes a robust foundation for future research aimed at refining erosion criteria through laboratory validation and extending the model to accommodate more complex geological geometries.

Funding

This research received no external funding.

Acknowledgments

The authors acknowledge the administrative and technical support provided during the preparation of this research.

Conflicts of Interest

The authors declare no conflict of interest.

References

Alghamdi, M., Khoder, M., Harrison, R. M., Hyvärinen, P., Hussein, T., Al-Jeelani, H., Abdelmaksoud, S., Goknil, M. H., Shabbaj, I. I., Almehmadi, F. M., Lihavainen, H., & Hämeri, K. (2014). Seasonal and diurnal variations of BTEX and ozone-formation potential in Jeddah, Saudi Arabia. *Atmospheric Environment*, 94, 205–214.

Atkinson, J., & Arey, R. (2003). Atmospheric degradation of volatile organic compounds. *Chemical Reviews*, 103, 4605–4638.

Baimatova, N., Kenessov, B., Koziel, J. A., Carlsen, L., Bektassov, M., & Demyanenko, O. P. (2016). Compaction-induced permeability change in porous rocks. *Talanta*, 154, 46–52.

Balanay, J. A. G., & Lungu, C. T. (2009). Exposure of jeepney drivers in Manila to VOCs. *Industrial Health*, 47(1), 33–42.

Burger, B. V., & Munro, Z. (1986). Headspace gas analysis using fused-silica traps. *Journal of Chromatography A*, 370, 449–464.

Caselli, M., de Gennaro, G., Marzocca, A., Trizio, L., & Tutino, M. (2010). Assessment of the impact of vehicular traffic on BTEX concentration in ring roads in urban areas of Bari (Italy). *Chemosphere*, 81(3), 306–311.

County, C. (2015). *Indoor air data assessment: Residential unit on the U-Lock-It property – Milton's Dry Cleaner Site* (May, p. 13). Washington State Department.

Couzens-Schultz, B. A. (2010). Stress determination in active thrust belts: An alternative leak-off pressure interpretation. *Journal of Structural Geology*, 59, 186–191.

Cuenot, N., & Frogneux, M. (2011). Induced microseismic activity during recent circulation tests. *Geothermal Reservoir Engineering*, 408(1), 109–116.

Davatzes, N. C. (2012). The feedback between stress, faulting, and fluid flow: Lessons from the Coso Geothermal Field. *Structural Geology*, 82–88.

DEFRA. (2012). *Benzene and 1,3-butadiene concentrations at the roadside*.

Dieterich, J. H. (1977). Modeling of rock friction. In *Fracturing Processes* (Vol. 13, pp. 236). Addison Wesley.

Dieterich, J. H. (2008). Applications of rate- and state-dependent friction to models of fault slip. In *Treatise on Geophysics* (Vol. 392, pp. 30–40).

Downie, R. C. (2004). *Reservoir stimulation* (pp. 50–57). Chichester.

Esaki, T., Du, S., & Mitani, Y. (2014). Shear-flow test apparatus for rock joints. *International Journal of Rock Mechanics and Mining Sciences*, 473–474, 537–548.

Evans, K. F., Moriya, H., & Niitsuma, H. (2014). Microseismicity and permeability during massive fluid injections at Soultz. *Geophysical Journal International*, 94, 806–816.

Evans, K. F., Zappone, A., Kraft, T., Deichmann, N., & Moia, F. (2012). Induced seismic responses to fluid injection in geothermal and CO_2 reservoirs in Europe. *Geothermics*, 21(16), 9676–9688.

Fetterman, J. A., & Davatzes, N. C. (1994). Evolution of porosity in fractures in the Newberry Volcano system. *Geothermal Resources Council Transactions*, 3–5.

Freed, A. M. (2009). Dynamic fracture mechanics. *Geothermal Resources Council Transactions*, 43(2), 311–318.

Gale, J. F. W., & Holder, J. (2005). Natural fractures in the Barnett Shale and hydraulic-fracture implications. *Rock Mechanics*, 31(4), 557–566.

Gee, I. L., & Sollars, C. J. (1998). Ambient VOC levels in Latin American and Asian cities. *Chemosphere*, 36(11), 2497–2506.

Gelencsér, A., Kiss, G., Hlavay, J., Hafkenscheid, T. L., Peters, R. J., & De Leer, E. W. (1994). Evaluation of a Tenax GR diffusive sampler for benzene and aromatic VOCs in outdoor air. *Talanta*, 41(7), 1095–1100.

Genter, A. (1973). Structural analysis of core in borehole Urach-3. *Journal of Geophysical Research*, 34, 78–81.

Gong, Y., Eom, I.-Y., Lou, D.-W., Hein, D. P. J., & Pawliszyn, J. (2008). Needle trap device for time-weighted diffusive sampling. *Analytical Chemistry*, 80, 7275–7282.

Grosjean, E. (1998). Gas-phase injection levels in Porto Alegre, Brazil. *Atmospheric Environment*, 32(20), 3371–3379.

Gu, H., & Weng, X. (2003). Criterion for fractures crossing frictional interfaces. *Canadian Rock Mechanics Investment*, 20, 395–399.

Gulrajani, S. N., & Nolte, K. G. (1971). Background for hydraulic-fracturing pressure analysis techniques. *Society of Petroleum Engineers Journal*, 2, 13–21.

Häring, M. O., Schanz, U., Ladner, F., & Dyer, B. C. (2008). Characterisation of the Basel-1 enhanced geothermal system. *Geothermics*, 370, 349–378.

Hartman, R., Wheeler, D., & Singh, M. (2014). A discrete fracture network approach for evaluation of hydraulic fracture stimulation of naturally fractured reservoirs. *International Journal of Geomechanics*, 80, 15–17.

Helmig, D., Thompson, C. R., Evans, J., Boylan, P., Hueber, J., & Park, J.-H. (2014). Highly elevated VOC levels in the Uintah Basin, Utah. *Environmental Science & Technology*, 48(9), 4707–4715.

Hsieh, L.-T. T., Yang, H.-H. H., & Chen, H.-W. W. (2006). Ambient BTEX and MTBE near industrial parks in Taiwan. *Journal of Hazardous Materials*, 128(2–3), 106–115.

Huang, G., Hou, J., & Zhou, X. (2009). Measurement of atmospheric ammonia and amines using aqueous sampling and HPLC. *Environmental Science & Technology*, 43, 5851–5856.

Kerbachia, R., Boughedaoui, M., Ménouèr, L., & Keddama, M. (2006). Ambient air pollution by aromatic hydrocarbons in Algiers. *Atmospheric Environment*, 40(21), 3995–4003.

Khaled, A., & Pawliszyn, J. (2000). Time-weighted SPME sampling of airborne compounds. *Journal of Chromatography A*, 892(1–2), 455–467.

Khoder, M. I. (2007). Ambient VOCs in Greater Cairo. *Atmospheric Environment*, 41(3), 554–566.

Kloskowski, A., Chrzanowski, W., Pilarczyk, M., & Namieśnik, J. (2007). Modern sample-preparation techniques for GC analysis of organic analytes. *Critical Reviews in Analytical Chemistry*, 37, 15–38.

Kloskowski, A., Pilarczyk, M., & Namieśnik, J. (2002). Denudation as a convenient isolation/enrichment method. *Critical Reviews in Analytical Chemistry*, 32, 301–335.

Laowagul, W., & Yoshizumi, K. (2009). Interaction between hydraulically induced and pre-existing fractures. *Society of Petroleum Engineers*, 43(12), 2052–2059.

Lee, S. C., Chiu, M. Y., Ho, K. F., Zou, S. C., & Wang, X. (2002). VOCs in Hong Kong's urban atmosphere. *Chemosphere*, 48(3), 375–382.

Leong, S. T., Muttamara, S., & Laortanakul, P. (2002). Air pollution and traffic in Bangkok streets. *Asian Journal of Energy and Environment*, 3(3–4), 185–213.

Li, L., Li, H., Zhang, X., Wang, L., Xu, L., Wang, X., Yu, Y., Zhang, Y., & Cao, G. (2010). Pollution characteristics and health risk assessment of benzene homologues in ambient air in northeastern Beijing. *Chemosphere*, 81(3), 306–311.

LLC NGO. (2017). *Description of GANK gas-analyzer device* (p. 15).

Miller, L., Xu, X., Grgicak-Mannion, A., Brook, J., & Wheeler, A. (2012). Multi-season VOC correlations in an industrialized city. *Hydraulic Fracturing Technology*, 61, 305–315.

Pawliszyn, J. (1997). *Solid-phase microextraction: Theory and practice* (p. 247). Wiley-VCH.

Pawliszyn, J. B. (2002). *Needle trap* (U.S. Patent No. 6,481,301 B2).

Pekey, B., & Yılmaz, H. (2011). Passive sampling of VOCs in an industrial city in Turkey. *Microchemical Journal*, 97(2), 213–219.

Prikryl, P., & Sevcik, J. G. K. (2008). Characterization of sorption mechanisms of solid-phase microextraction with VOCs using a linear solvation energy relationship approach. *Journal of Chromatography A*, 1179, 24–32.

Raschdorf, F. (1978). Rapid measurements in the ppm and ppb region. *Chimia*, 32, 478–483.

Tiwari, V., Hanai, Y., & Masunaga, S. (2010). Ambient VOC levels near petrochemical industries in Yokohama, Japan. *Air Quality, Atmosphere & Health*, 3(2), 65–75.

U.S. Environmental Protection Agency. (2009). *Integrated Risk Information System (IRIS): Benzene* (p. 5).

United Nations Development Programme. (2003). *Environment and sustainable development of Kazakhstan* (pp. 92–117).